




Article

Coordination Polymers Based on a Biphenyl Tetraphosphonate Linker: Synthesis Control and Photoluminescence

Ana D. G. Firmino ^{1,2,†}, Ricardo F. Mendes ^{1,†} , Duarte Ananias ^{1,3} , Jéssica S. Barbosa ^{1,2}, João P. C. Tomé ^{2,4} and Filipe A. Almeida Paz ^{1,*} 

¹ Department of Chemistry, CICECO—Aveiro Institute of Materials, University of Aveiro, 3810-193 Aveiro, Portugal; danielafirmino1@ua.pt (A.D.G.F.); rfmendes@ua.pt (R.F.M.); dananias@ua.pt (D.A.); jessicambarbosa@ua.pt (J.S.B.)

² QOPNA and LAQV-REQUIMTE, Department of Chemistry, University of Aveiro, 3810-193 Aveiro, Portugal; jtome@tecnico.ulisboa.pt

³ Department of Physics, CICECO—Aveiro Institute of Materials, University of Aveiro, 3810-193 Aveiro, Portugal

⁴ CQE and Departamento de Engenharia Química Instituto Superior Técnico, Universidade de Lisboa Av. Rovisco Pais, no 1, 1049-001 Lisboa, Portugal

* Correspondence: filipe.paz@ua.pt; Tel.: +351-234-401418

† These authors contributed equally to this work.

Academic Editor: Alessandro Stroppa

Received: 25 March 2020; Accepted: 15 April 2020; Published: 16 April 2020



Abstract: In this work, we used the rigid tetrapodal organic linker, [1,1'-biphenyl]-3,3',5,5'-tetrayltetrakis(phosphonic acid) (H_8btp), for the preparation of two lanthanide–organic framework families of compounds: layered $[Ln_7(H_5btp)_4(H_{5,5}btp)_2(H_6btp)_2(H_2O)_{12}] \cdot 23.5H_2O \cdot MeOH$ [where $Ln^{3+} = Eu^{3+}$ (**1Eu**) and Gd^{3+} (**1Gd**)], prepared using microwave-irradiation followed by slow evaporation; 3D $[Ln_4(H_3btp)(H_4btp)(H_5btp)(H_2O)_8] \cdot 3H_2O$ [where $Ln^{3+} = Ce^{3+}$ (**2Ce**), Pr^{3+} (**2Pr**), and Nd^{3+} (**2Nd**)], obtained from conventional hydro(solvo)thermal synthesis. It is shown that in this system, by carefully selecting the synthetic method and the metal centers, one can increase the dimensionality of the materials, also increasing structural robustness (particularly to the release of the various solvent molecules). Compound **1** is composed of 2D layers stacked on top of each other and maintained by weak π – π interactions, with each layer formed by discrete 1D organic cylinders stacked in a typical brick-wall-like fashion, with water molecules occupying the free space in-between cylinders. Compound **2**, on the other hand, is a 3D structure with small channels filled with crystallization water molecules. A full solid-state characterization of **1** and **2** is presented (FT-IR spectroscopy, SEM microscopy, thermogravimetric studies, powder X-ray diffraction and thermodiffraction). The photoluminescence of **1Eu** was investigated.

Keywords: metal-organic framework; crystal structure; photoluminescence

1. Introduction

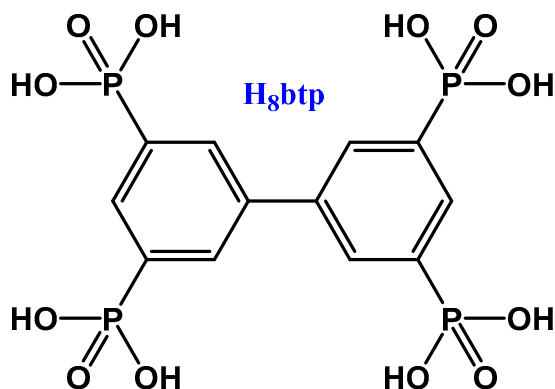
Metal-Organic Frameworks (MOFs), or Porous Coordination Polymers (PCPs), are a class of crystalline materials built from the coordination of organic linkers to metal ions or clusters [1]. Among the assorted reasons why there are so many reports in the area of MOFs and PCPs, and why they remain an attractive topic of research, one can point out their tunable chemical structure and/or their multifunctional properties [2]. The ability to design a network with specific pore sizes and shapes is one of the main features why these materials are good candidates for multiple applications in

different research areas like gas storage and separation [3,4], catalysis [5,6], sensing [7–11], and drug delivery [12,13], among others [14–21].

While the main research regarding MOFs remains focused on materials derived from *d*-block metals coordinated to carboxylate-based organic linkers, our research group has focused on metal phosphonates, more specifically, lanthanide phosphonate-based MOFs (LnOFs). LnOFs have gained particular interest, in some part due to the possibility to design new materials by changing the lanthanide radii. In some particular cases, the LnOFs properties can also change [22–24]. Recently, Wang and co-workers were able to improve the DNA sensing of LnOF nanosheets by simple change in lanthanide ions [25]. The contraction of ionic radii led to a lower quenching efficiency. Tetraphosphonic organic linkers have gained particular interest in recent years, especially phosphonic acids based on tetraphenylmethane and tetraphenylsilane building units. [26] While their geometries can pose some challenges regarding its synthetic approaches (mainly due to the high rigidity that these molecules present), it results in their properties improvement. A particular improvement is the stability of these materials: while many MOFs show low stability in even ambient conditions, some of these materials can withstand solutions of concentrated acids (HCl and H₂SO₄) and even *aqua regia* [27]. In our group, the rich chemistry of phosphonic acid allowed the preparation of a variety of structures ranging from 1D to 3D networks by, in many cases, slight changes in experimental conditions. With this we were able to synthesize MOFs with a broad range of applications: from photoluminescence [28–30], to luminescent thermometers [31], heterogeneous catalyst [32,33] and/or proton conductors [34].

In previous reports we presented and explored the phosphonic acid [1,1'-biphenyl]-3,3',5,5'-tetrakis(phosphonic acid) (H₈btp) as a new tetraphosphonic organic ligand (Scheme 1) [28,31,34]. H₈btp afforded a particular series of MOF-type compounds self-assembled from La³⁺ cations (or mixtures of lanthanides), which then showed not only fascinating structural features, but interesting photoluminescent properties. We also registered, however, that these 2D materials presented a significant drawback (which might also be seen as a disadvantage regarding a future practical application): their thermal stability was very low with the framework being only stable between ambient temperature and ca. 70 °C. In order to try to overcome this disadvantage, we have further explored the chelating ability of H₈btp under different synthetic conditions, including a careful selection of the lanthanide radii, and isolated two new isotypical families of LnOFs which we report here:

- (i) layered [Ln₇(H₅btp)₄(H_{5,5}btp)₂(H₆btp)₂(H₂O)₁₂]·23.5H₂O·MeOH [where Ln³⁺ = Eu³⁺ (**1Eu**) and Gd³⁺ (**1Gd**)] (prepared using the same self-assembly methodology previously reported for the materials based on La³⁺ and H₈btp, i.e., microwave-irradiation followed by slow evaporation);
- (ii) 3D [Ln₄(H₃btp)(H₄btp)(H₅btp)(H₂O)₈]·3H₂O [where Ln³⁺ = Ce³⁺ (**2Ce**), Pr³⁺ (**2Pr**), and Nd³⁺ (**2Nd**)], obtained from conventional hydro(solvo)thermal synthesis. This approach allowed us to obtain a material with increased dimensionality (3D) in a much less synthesis time.



Scheme 1. Schematic representation of the organic linker [1,1'-biphenyl]-3,3',5,5'-tetrakis(phosphonic acid) (**H₈btp**) used in this work.

2. Results and Discussion

2.1. Crystal Structure Details

2.1.1. $[\text{Ln}_7(\text{H}_5\text{btp})_4(\text{H}_{5.5}\text{btp})_2(\text{H}_6\text{btp})_2(\text{H}_2\text{O})_{12}] \cdot 23.5\text{H}_2\text{O} \cdot \text{MeOH}$ (1)

The structure of **1** was unveiled while studying single-crystals of $[\text{Eu}_7(\text{H}_5\text{btp})_4(\text{H}_{5.5}\text{btp})_2(\text{H}_6\text{btp})_2(\text{H}_2\text{O})_{12}] \cdot 23.5\text{H}_2\text{O} \cdot \text{MeOH}$ (**1Eu**) using X-ray diffraction. The isotypical nature of **1Eu** and **1Gd** was unequivocally confirmed by powder X-ray diffraction data (Figures S1 and S2 in the Supporting Information), being supported by EDS mapping (Figures S8 and S9 in the Supporting Information). The family crystallizes in the monoclinic space group $P2_1/c$, with a large asymmetric unit composed of three and half metal centers and four different $\text{H}_{8-x}\text{btp}^{x-}$ residues ($x = 2, 2.5$ and 3). Structural adhesion is overall achieved by a complex network of hydrogen bonding interactions between the phosphonate groups and the several solvent molecules.

The four metal centers have different coordination numbers as depicted in Figure 1. Eu1 is at a center of inversion, with multiplicity of 2, being hexacoordinated to six phosphonate groups, while Eu2 is heptacoordinated to five different phosphonate groups and two coordination water molecules (O2W and O3W are disordered). The remaining two metal centers, Eu3 and Eu4 are also heptacoordinated to two coordination water molecules and five phosphonate groups, each. For the former two coordination environments, the phosphonate groups coordinate with the metal centers with the same $k^1\text{-O}$ mode of coordination while for the last two, besides this mode of coordination, two phosphonate groups have a $k^2\text{-O}$ coordination mode. The Eu–O bond lengths were found in the 2.221(7)–2.535(16) Å range, comparable to those reported for other Ln^{3+} -based phosphonate compounds, and the internal O–La–O polyhedral angles are in the 69.5(4)–180.0(2)° range (Table S1 in the Supporting Information).

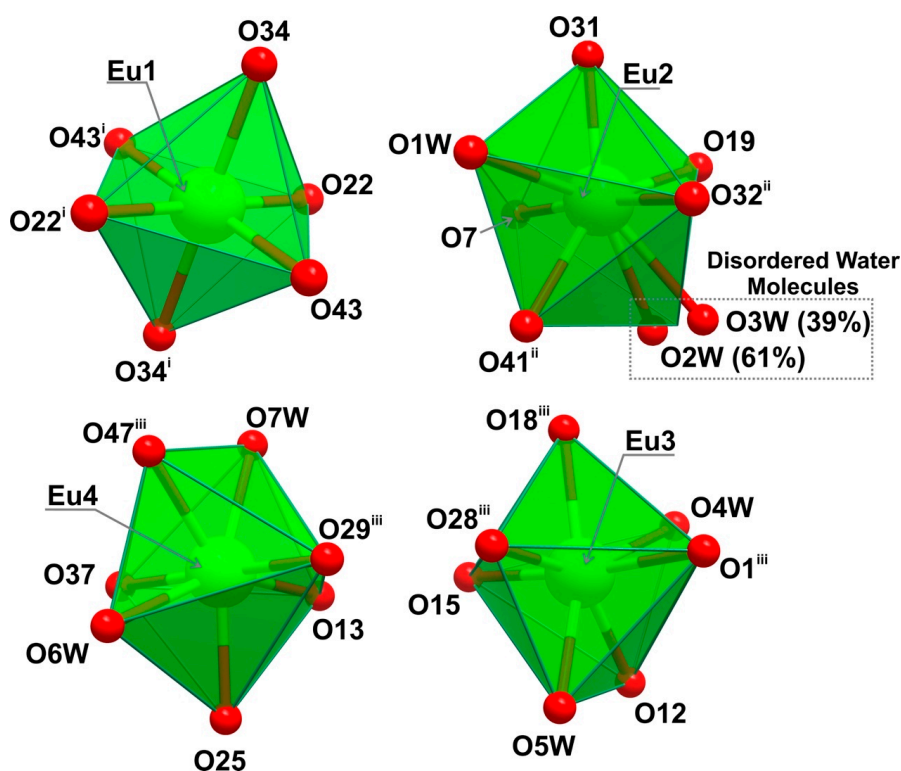


Figure 1. Polyhedral representation of the four distorted Eu^{3+} coordination environments present in the crystal structure of $[\text{Eu}_7(\text{H}_5\text{btp})_4(\text{H}_{5.5}\text{btp})_2(\text{H}_6\text{btp})_2(\text{H}_2\text{O})_{12}] \cdot 23.5\text{H}_2\text{O} \cdot \text{MeOH}$ (**1Eu**). Table S1 (in the Supporting Information) gather all the geometrical details on the represented bond lengths, angles. Symmetry transformations used to generate equivalent atoms: (i) $-x, 1-y, 1-z$; (ii) $-x, 1-y, -z$; (iii) $x, 3/2-y, -1/2+z$.

The phosphonic acid groups have three different protonation degrees: -3 , -2.5 or -2 . The partial protonation arises from the need to balance the overall crystal charge, and the location of the respective hydrogen atom was carefully selected and placed on O45 (based on proximity of hydrogen bonding acceptor). We further note that the structure also has hydrogen atoms which “jump” between adjacent phosphonate groups, namely between O23 and O30 and between O33 and O38.

As observed for the previously reported $[\text{Ln}_4(\text{H}_6\text{btp})_2(\text{H}_4\text{btp})_2(\text{H}_8\text{btp})(\text{H}_2\text{O})_{16}] \cdot 12\text{H}_2\text{O}$ isotypical family of networks [where $\text{Ln}^{3+} = \text{La}^{3+}$, $(\text{La}_{0.9}\text{Eu}_{0.1})^{3+}$ and $(\text{La}_{0.9}\text{Tb}_{0.1})^{3+}$] [28], **1** contains discrete 1D organic cylinders stacked in a typical brick-wall-like fashion in the bc plane, with solvent molecules occupying the available space in-between these cylinders as depicted in Figure 2. Connections between the organic cylinders are ensured by metallic dimers (*inset* in Figure 2a), leading to 2D layers placed in the ac plane of the unit cell, stacked on top of each other and maintained by weak π - π interactions between the aromatic rings of adjacent layers [distance of $3.982(6)\text{\AA}$ and dihedral angle of $13.3(5)^\circ$].

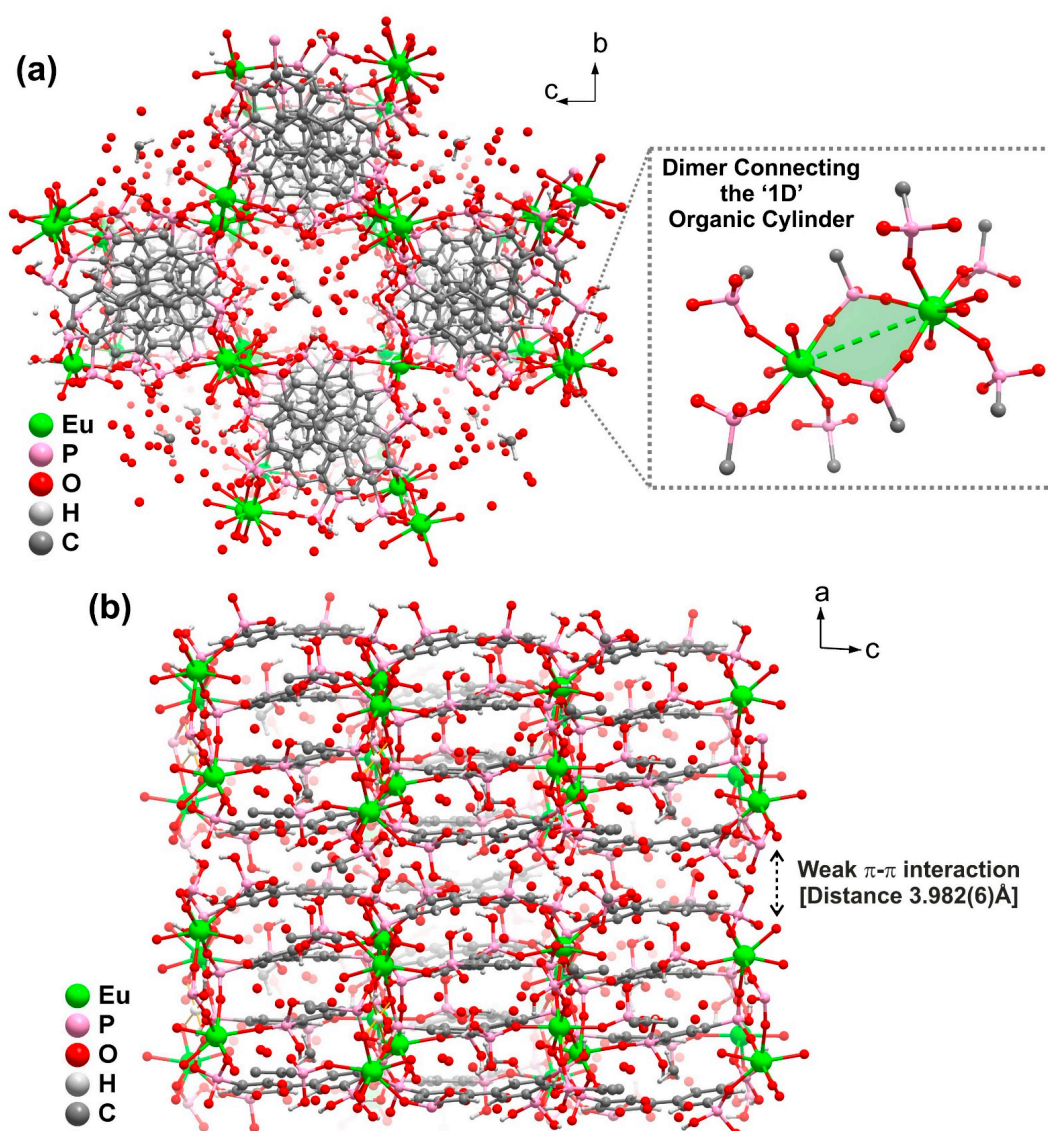


Figure 2. Crystal packing of $[\text{Eu}_7(\text{H}_5\text{btp})_4(\text{H}_{5.5}\text{btp})_2(\text{H}_6\text{btp})_2(\text{H}_2\text{O})_{12}] \cdot 23.5\text{H}_2\text{O} \cdot \text{MeOH}$ (**1Eu**) viewed in perspective along the (a) [100] and (b) [010] directions of the unit cell. The representations emphasize simultaneously the presence of several dimers formed by the metal centers and the phosphonic acid groups that connects the “1D” organic cylinders of **1Eu**.

Within these cylinders the organic linkers are stacked on top of each other with an overall rotation angle of ca. 135° along the [100] direction, forming a double-helix-like structural motif as depicted in Figure 3. Besides the connection to the metal centers, each organic residue forms weak π - π interactions between each other, with intercentroid distances ranging from 3.5805(4) to 3.8321(5) Å [dihedral angles between 4.8(4) and 6.1(5)°].

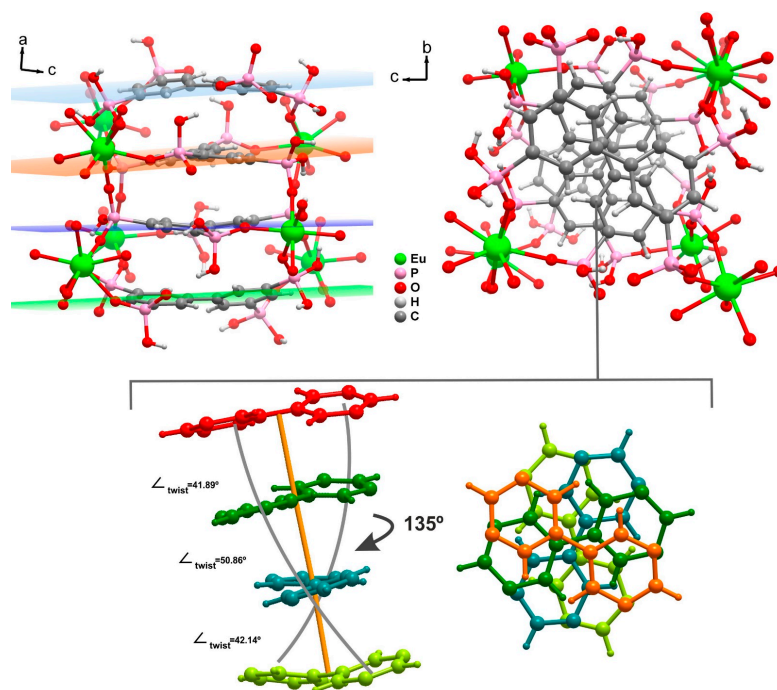


Figure 3. Schematic representation of the organic cylinder present in the crystal structure of $[\text{Eu}_7(\text{H5btp})_4(\text{H5.5btp})_2(\text{H6btp})_2(\text{H}_2\text{O})_{12}] \cdot 23.5\text{H}_2\text{O} \cdot \text{MeOH}$ (1Eu) viewed along the [010] and [100] directions of the unit cell. The schemes emphasize the close packing of the organic linkers, with inter-planar distances ranging between 3.5805(4) and 3.8321(5) Å. On the right there is a representation of the same organic skeleton in the cylinder emphasizing the close packing and rotation along the *a*-axis of the four composing aromatic cores.

The presence of several phosphonate groups and coordinated and crystallization solvent molecules promote the formation of a complex network of hydrogen-bonding interactions. Within the organic cylinders, such interactions are of the P-O...H-O-P type (i.e., inter-phosphonate groups) being rather strong and directional [$d_{D...A}$ distances between 2.496(13) and 3.263(13) Å with \langle (DHA) between 125–176°]. These ensure a close packing of the 2D layers and overall structural integrity of **1** (for more details see Table S2 in the Supporting Information).

It is interesting to note that the four independent organic linkers composing the aforementioned organic cylinder connect, each, to a different number of metal centers (3, 4, 5 and 6), ultimately leading to the 2D compact network which can be more easily analyzed from a pure topological perspective. Figure S13 (in the Supporting Information) depicts the reduction of the network to simple nodes (i.e., the metal centers) and bridges (ensured by the organic linkers). Following the recommendations of Alexandrov et al. [35], who suggested that any moiety (ligand or atoms) connecting more than two metallic centers should be considered as a network node. For this case, both the metal centers and the organic linkers were considered as network nodes. We note that the hydrogen bonds were not included in these calculations. The network of the isotypical family of **1** is, therefore, an octanodal 3,4,5,5,5,5,6,6-connected network with total point symbol $\{4^{13} \cdot 6^2\}_2 \{4^3\}_2 \{4^5 \cdot 6^3 \cdot 8^2\}_6 \{4^6 \cdot 8^8 \cdot 10\} \{4^6\}_2 \{4^9 \cdot 6\}_2$ as revealed by the software package TOPOS [36]. Database review of the *Reticular Chemistry Structure Resource* (RCSR) [37] and in EPINET [38] show that this complex topology has not been described yet.

We note that the network was attempted to be reduced to more simple nodes such as those described in the paper by Bonneau et al. [39]. However, this approach did not significantly reduce the number of nodes ultimately leading instead to a mixture of different node approaches, hence in this manuscript we decided to maintain the classical approach. For this case, the notations $\{4^3\}$, $\{4^9 \cdot 6\}$, $\{4^6\}$ correspond to the three $H_{8-x}btp^{x-}$ residues and $\{4^{13} \cdot 6^2\}$, $\{4^5 \cdot 6^3 \cdot 8^2\}$, $\{4^6 \cdot 8^8 \cdot 10\}$ corresponds to the metal centers.

2.1.2. $[Ln_4(H_3btp)(H_4btp)(H_5btp)(H_2O)_8] \cdot 3H_2O$ (2)

The structure of the isotypical family of compounds $[Ln_4(H_3btp)(H_4btp)(H_5btp)(H_2O)_8] \cdot 3H_2O$ [where $Ln^{3+} = Ce^{3+}$ (**2Ce**), Pr^{3+} (**2Pr**), and Nd^{3+} (**2Nd**)] was elucidated for the La^{3+} -based material. Besides elemental analysis (see Experimental Section), the homogeneity of the bulk samples was studied using powder X-ray diffraction (Figures S1 and S3 in the Supporting Information), FT-IR spectroscopy (Figure S7 in the Supporting Information), and electron microscopy (Figures S10 to S12 in the Supporting Information).

Compound **2** crystallizes in the monoclinic space group $P2_1/c$, with the asymmetric unit being composed of four metal centers and three different $H_{8-x}btp^{x-}$ residues ($x = 5, 4$ and 3). The four metal centers have different coordination numbers (Figure 4): La1 and La2 are both octacoordinated to five phosphonate groups and three coordination water molecules; La3 is nonacoordinated to seven different phosphonate groups and two coordination water molecules; La4 is heptacoordinated to six different phosphonate groups and one coordination water molecule. As expected, and compared with the structure of **1**, the overall coordination numbers are higher, thus reflecting the larger ionic radius of the metal centers. The La–O bond lengths were found in the 2.346(5)–2.851(6) Å range while the internal O–La–O polyhedral angles are in the 53.61(15)–59.40(15)° range (see Table S3 in the Supporting Information).

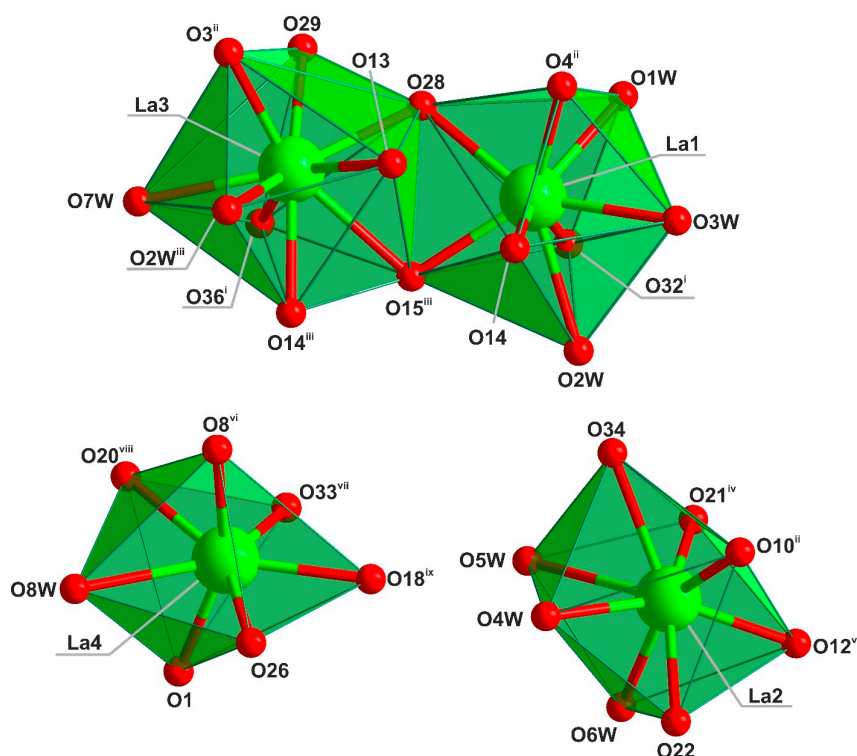


Figure 4. Polyhedral representation of the distorted coordination environments present in the crystal structure of $[La_4(H_5btp)(H_4btp)(H_3btp)(H_2O)_8] \cdot 3H_2O$ (**2La**). See Table S1 for geometrical details on the represented bond lengths and angles. Symmetry transformation used to generate equivalent atoms: (i) $-x + 1, y - 1/2, -z + 3/2$; (ii) $x + 1, y, z$; (iii) $-x + 1, -y, -z + 1$; (iv) $-x + 1, -y + 1, -z + 1$; (v) $-x, -y + 1, -z + 1$; (vi) $x + 1, -y + 1/2, z + 1/2$; (vii) $x - 1, y, z$; (viii) $x - 1, -y + 1/2, z + 1/2$; (ix) $x, -y + 1/2, z + 1/2$.

When compared to the previously described layered material, **2** has a smaller number of organic linkers in the asymmetric unit: a total of three, showing distinct protonation degrees -5 , -4 and -3 . The overall structural connectivity of each linker is distinct: one acts as a hexadentate bridge, connecting six metal centers, while the remaining residues act as a hepta- and octadentate linkers, connecting seven and eight metal centers each. For the former case, the phosphonate groups coordinate to the metal centers by simple k^1-O coordination modes, while in the latter two situations there are also k^2-O and $\mu-O,O$ modes of coordination involved. It is noteworthy to mention that when compared to the structural features of the organic linkers in **1**, one can easily infer that the bridges can easily accommodate more metal centers in the structure by increasing the overall connectivity and having, in average, a higher level of deprotonation.

The network of **2** is also composed by organic cylinders distributed in typical brick-wall-like fashion in the ab plane and formed by stacked organic linkers along $[001]$ direction of the unit cell (Figure 5). The organic linkers are stacked, as depicted in Figure 6, on top of each other with a rotation angle of ca. 92° along the $[100]$ direction, forming a double-helix-like structural motif, just as observed in the other related materials. As so, besides the connection with the metallic centers (described below), the organic linkers are further engaged in weak $\pi-\pi$ interactions with intercentroid distances ranging between $3.5545(5)$ and $3.9692(5)$ Å [dihedral angles between 4 and 9°] (Figure 6).

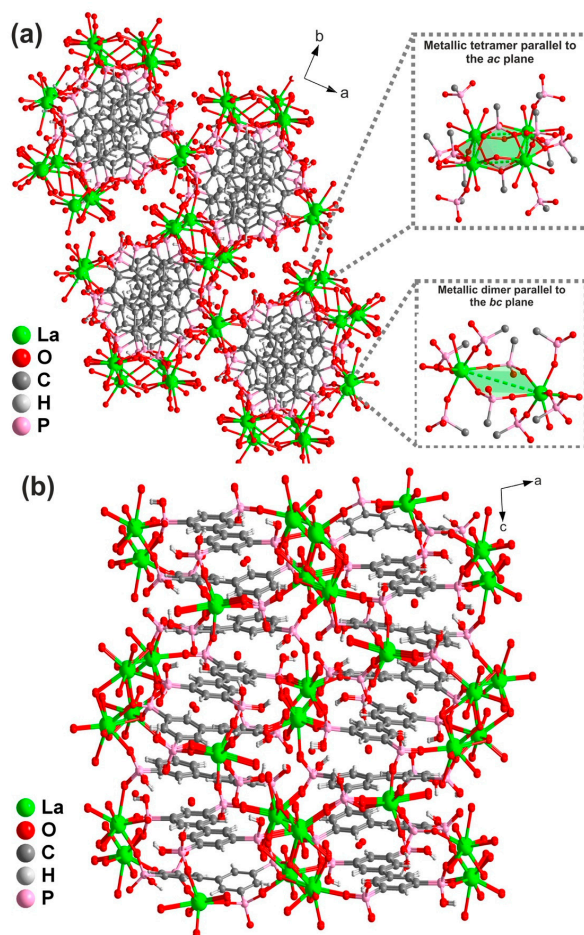


Figure 5. Crystal packing of $[\text{La}_4(\text{H}_5\text{btp})(\text{H}_4\text{btp})(\text{H}_3\text{btp})(\text{H}_2\text{O})_8]\cdot 3\text{H}_2\text{O}$ (**2La**) viewed in perspective along the (a) $[001]$ and (b) $[010]$ directions of the unit cell. The representations also emphasize, simultaneously, not only the presence of a metallic dimer formed by two metal centers and the phosphonic acid groups, responsible for the connection between the “1D” cylinders along the $[100]$ direction, but also the presence of a metallic tetramer which connects the same cylinders along the $[010]$ direction.

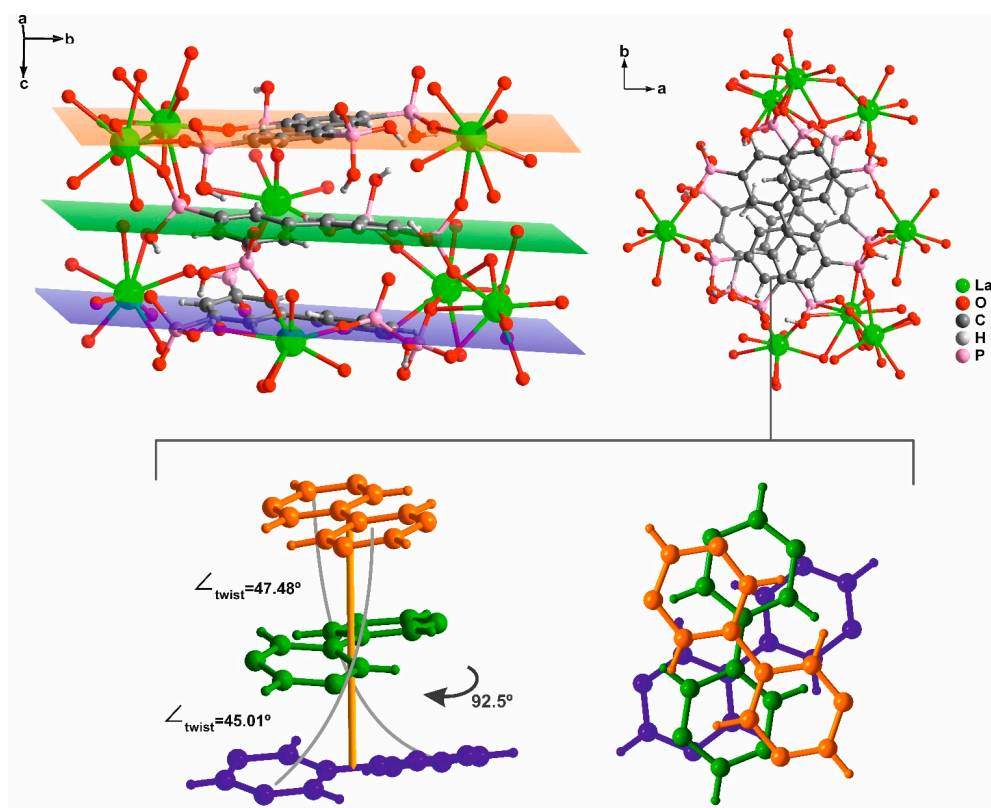


Figure 6. Schematic representation of the organic cylinder present in the crystal structure of $[\text{La}_4(\text{H}_5\text{btp})(\text{H}_4\text{btp})(\text{H}_3\text{btp})(\text{H}_2\text{O})_8]\cdot 3\text{H}_2\text{O}$ (**2La**). The schemes emphasize the close packing of the organic linkers, with inter-planar distances ranging between 3.5545(5) and 3.9692(5) Å. On the right there is a representation of the same organic skeleton in the cylinder emphasizing the close packing and rotation along the *a*-axis of the three aromatic cores.

As for **1**, these cylinders are mutually connected by metallic dimers. However, unprecedented tetrameric units are also present for this family of compounds (*insets* in Figure 5a). Intermetallic distances: for the dimer, $\text{La}2 \cdots \text{La}2$ of 6.0643(6) Å; for the tetramer, $\text{La}1 \cdots \text{La}3$ of 4.0834(4) Å and 4.4179(5) Å. These metallic connections (covalent bonds), allied to very strong and directional hydrogen-bonding interactions between phosphonate groups [$d_{D \cdots A}$ distances between 2.521(7) and 2.842(8) Å with $\angle(\text{DHA})$ between 111 and 172°—see Table S4 in the Supporting Information], are the main reason for the formation of the three-dimensional network of the MOF structure **2** as shown in Figure 5b.

Overall, this family of compounds has a lower number of both coordinated and crystallization solvent molecules. We note that these are also engaged in strong hydrogen bonding interactions with the phosphonate groups lining the inner walls of the channels of the network [$d_{D \cdots A}$ distances between 2.553(9) and 3.013(8) Å with $\angle(\text{DHA})$ between 131 and 161°—see Table S4 in the Supporting Information].

Using the same topological strategy previously described for **1** (again, the hydrogen bonds were not included in the calculation), this new MOF structure is a new hexanodal 5,6,6,7,7,8-connected network with total point symbol $\{3\cdot 4^{12}\cdot 6^2\}\{3^2\cdot 4^{10}\cdot 6^9\}\{3^4\cdot 4^{16}\cdot 5^6\cdot 6^2\}\{3^7\cdot 4^{11}\cdot 5^3\}_2\{4^4\cdot 5\cdot 6\cdot 8^9\}\{4^8\cdot 6^2\}$ (see Figure S14 in the Supporting Information), wherein $\{3\cdot 4^{12}\cdot 6^2\}$, $\{3^2\cdot 4^{10}\cdot 6^9\}$, $\{3^4\cdot 4^{16}\cdot 5^6\cdot 6^2\}$ and $\{3^7\cdot 4^{11}\cdot 5^3\}$, $\{4^4\cdot 5\cdot 6\cdot 8^9\}$, $\{4^8\cdot 6^2\}$ notations correspond to the metal centers and $\text{H}_{8-x}\text{btp}^{x-}$ residues, respectively. We note that in this framework La1 and La3 exhibit the same point and extended symbol being, thus, equivalent hence the six-connectivity nature of the network.

2.2. Structural Characterization

2.2.1. Thermogravimetry

The thermal stability of $[\text{Gd}_7(\text{H}_5\text{btp})_4(\text{H}_{5.5}\text{btp})_2(\text{H}_6\text{btp})_2(\text{H}_2\text{O})_{12}] \cdot 23.5\text{H}_2\text{O} \cdot \text{MeOH}$ (**1Gd**) was investigated between ambient temperature and ca. 800 °C, providing additional information on the hydration level of this family of isotypical compounds. As depicted in Figure S4, the thermogram for compound **1Gd** shares many similarities with that of $[\text{La}_4(\text{H}_6\text{btp})_2(\text{H}_4\text{btp})_2(\text{H}_8\text{btp})(\text{H}_2\text{O})_{16}] \cdot 12\text{H}_2\text{O}$ [28], ultimately indicating a comparable thermal behavior. For **1Gd** the thermogram does not evidence unequivocal regions in which the mass remains stable. There is a continuous weight loss (more significant at some specific temperatures) over the entire temperature range. This behavior creates additional difficulties for individual assignments of temperature range *vs.* released residues, although it was foreseeable that this should happen due to the large number of coordination and crystallization solvent molecules present in the structure. One can, nevertheless, confirm the crystallographic studies for this compound. It is possible to discern three main weight losses: the first, between ambient temperature and ca. 100 °C, corresponding to 8.2% of the total weight loss, is attributed to the release of all crystallization solvent molecules from the structure (calculated 8.2%), i.e., the 23.5 water molecules plus the one methanol molecule. Above this temperature, there is an immediate second weight loss until ca. 200 °C. In this temperature range, the coordination water molecules are removed from the structure corresponding to a total weight loss of 4.3% (calculated 3.9%). The final step corresponds to the decomposition of the organic component.

The thermal behavior of the bulk $[\text{Ln}_4(\text{H}_3\text{btp})(\text{H}_4\text{btp})(\text{H}_5\text{btp})(\text{H}_2\text{O})_8] \cdot 3\text{H}_2\text{O}$ (**2**) materials were also investigated between ambient temperature and ca. 800 °C. Due to the isotypical nature of the compounds the following paragraph discussion will be solely focused on compound **2Ce** (see Figure S5 in the Supporting Information). For **2Ce**, one discerns three main weight losses. The first, between ambient temperature and ca. 110 °C, corresponding to 2.4% of the total weight loss, is attributed to the release of all crystallization solvent molecules (calculated 2.4%), i.e., a total of 3 water molecules. We emphasize that this value agrees well with the water content found from the performed crystallographic studies. Above this temperature, there is a second weight loss until ca. 250 °C. In this temperature range, the coordination water molecules are removed from the structure (in this case the observed 6.6% weight loss is equivalent to eight water molecules). The final step corresponds to the decomposition of the organic content.

Variable-temperature powder X-ray diffraction studies on $[\text{Ce}_4(\text{H}_3\text{btp})(\text{H}_4\text{btp})(\text{H}_5\text{btp})(\text{H}_2\text{O})_8] \cdot 3\text{H}_2\text{O}$ (**2Ce**) further corroborate the aforementioned assumptions concerning the release of water molecules and phase modifications (Figure S5 – *top* – see the Supporting Information): from ambient temperature to ca. 300 °C the structure changes, leading to the formation of a new crystalline phase as a consequence of the release of crystallization and coordination water molecules. The crystalline structure starts to collapse above this temperature becoming almost fully amorphous at 550 °C.

While these compounds share many structural similarities, the MOF compound **2** shows superior framework stability when compared to the previously reported $[\text{Ln}_4(\text{H}_6\text{btp})_2(\text{H}_4\text{btp})_2(\text{H}_8\text{btp})(\text{H}_2\text{O})_{16}] \cdot 12\text{H}_2\text{O}$ [28] and the herein reported $[\text{Ln}_7(\text{H}_5\text{btp})_5(\text{H}_6\text{btp})_3(\text{H}_2\text{O})_{12}] \cdot 23.5\text{H}_2\text{O} \cdot \text{MeOH}$ (**1**) materials that became both amorphous at rather low temperatures. We attribute this feature to the increased connectivity between metal ions and organic linkers: in **2** the structure contains less solvent molecules, both coordinated and of crystallization, and a higher connectivity of the phosphonate groups; thus, the liberation of the solvent molecules, including those which may be coordinated to the metal centers and pointing towards the small channels of the network, do not promote such an earlier onset decomposition of the material, with crystalline material being observed at temperature as high as 450 °C (see *inset* in Figure S5 in the Supporting Information).

2.2.2. FT-IR Spectroscopic Studies

The vibrational FT-IR spectroscopy studies support the structural features unveiled by the X-ray diffraction studies. Figures S5 and S6 (in the Supporting Information) show the FT-IR spectra of the materials in the 3650–350 cm^{-1} spectral region, including assignments for each of the main observed bands. Because **1** and **2** have the same functional groups, the spectra contain the same vibrational modes. A broad band is centered in the ca. 3600–2550 cm^{-1} spectral range, being attributed to both $\nu(\text{O-H})$ stretching vibrational modes from coordination and crystallization water molecules and to the $\nu(\text{PO-H})$ stretching vibration of the phosphonate groups. In the central region of the spectrum, between ca. 1745 and 1560 cm^{-1} , it is possible to observe the typical $\nu(\text{C=C})$ stretching vibrational modes arising from the aromatic rings and the deformation stretching of the water molecules. We further observe a sharp vibrational mode at ca. 695 cm^{-1} , corresponding to the $\nu(\text{P-C})$ stretching vibration. Also, in this region, the stretching vibrational modes of $\nu(\text{P=O})$ were noticed from ca. 1300–1060 cm^{-1} , and those of $\nu(\text{P-O})$ from ca. 1070 to 830 cm^{-1} .

2.3. Photoluminescence Studies

The excitation spectra of **1Eu** were recorded at ambient temperature (ca. 300 K) and 12 K monitoring the strongest $\text{Eu}^{3+} {}^5\text{D}_0 \rightarrow {}^7\text{F}_2$ emission transition (Figure 7). Both spectra are dominated by a broad UV band (240–320 nm) attributed to $\pi-\pi^*$ transitions of the organic ligands, which are very similar to the one previous reported for the Ln^{3+} MOFs obtained with the H_8btp organic linker [28–31]. The additional sharp lines in the spectra of **1Eu** are ascribed to the intra- $4f^6 {}^7\text{F}_{0,1} \rightarrow {}^5\text{D}_{1-4}$, ${}^5\text{L}_6$, ${}^5\text{G}_{2-6}$ and ${}^5\text{H}_{3-7}$ transitions of Eu^{3+} . The strong improvement of the 240–320 nm broad band, when the temperature decreases, demonstrates a non-effective energy transfer from the ligand to the Eu^{3+} ions (*antenna effect*) at the ambient temperature.

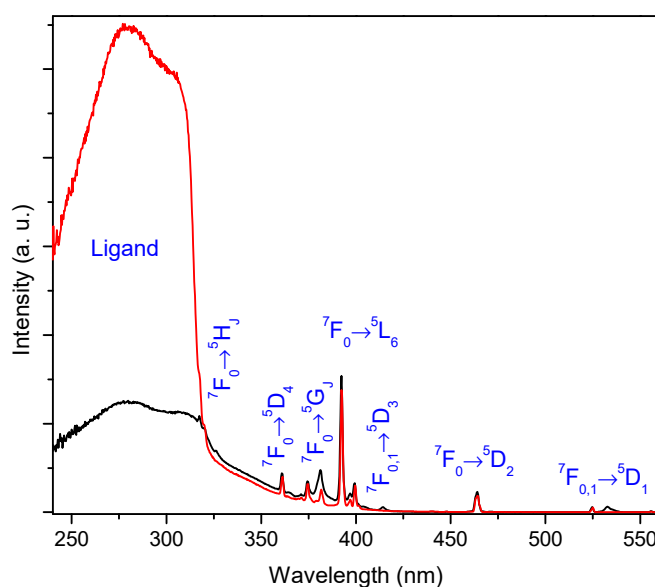


Figure 7. Excitation spectra of $[\text{Eu}_7(\text{H}_5\text{btp})_4(\text{H}_{5,5}\text{btp})_2(\text{H}_6\text{btp})_2(\text{H}_2\text{O})_{12}] \cdot 23.5\text{H}_2\text{O} \cdot \text{MeOH}$ (**1Eu**), recorded at ambient temperature (black line) and at 12 K (red line), while monitoring the Eu^{3+} emission at 610.5 nm.

The emission spectra of **1Eu** recorded at ambient temperature and 12 K, excited at 393 nm are presented in Figure 8. The sharp Eu^{3+} emission lines are assigned to the ${}^5\text{D}_0 \rightarrow {}^7\text{F}_{0-4}$ transitions. The ${}^5\text{D}_1 \rightarrow {}^7\text{F}_{0-3}$ transitions are only properly noticed, even at 12 K, after magnification (Figure S15 in the Supporting Information), demonstrating an efficient relaxation between the ${}^5\text{D}_1$ and ${}^5\text{D}_0$ excited states promoted by the vibrations of the organic linkers and the coordinated water molecules. The dominance of the ${}^5\text{D}_0 \rightarrow {}^7\text{F}_2$ over the ${}^5\text{D}_0 \rightarrow {}^7\text{F}_1$ transition is typical of Eu^{3+} environments without inversion center.

Although, the structure of **1Eu** presents four independent Eu^{3+} crystal sites, one of which in an inversion center, the corresponding emission spectra do not allow discriminating the corresponding individual photoluminescence signatures. Nevertheless, changing the excitation wavelength from 393 to 310 nm at 12 K (inset of Figure 8) results on a substantial change on the emission profile, particularly on the ${}^5\text{D}_0 \rightarrow {}^7\text{F}_1$ transition region. The emission spectrum obtained with the 310 nm excitation, in addition to the three lines of the 393 nm spectrum shows four additional Stark components, which is in good agreement with the presence of multiple Eu^{3+} local sites. In accordance, the ${}^5\text{D}_0$ decay curve of **1Eu** under direct excitation at 393 nm (${}^5\text{L}_6$ excited level), while monitoring the strongest ${}^7\text{F}_2$ Stark component at ambient temperature (Figure S16 in the Supporting Information), cannot be properly described by a single-exponential function. The data is only well fitted by a second order exponential function yielding lifetimes of 0.39 ± 0.01 and 1.16 ± 0.10 ms, with an average lifetime of 0.52 ms (details in the Supporting Information).

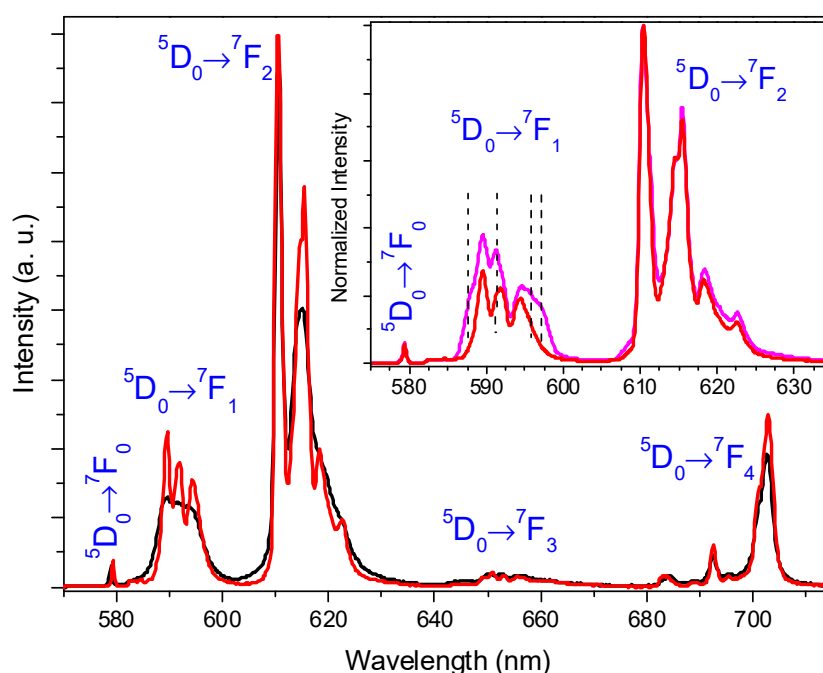


Figure 8. Emission spectra of $[\text{Eu}_7(\text{H}_5\text{btp})_4(\text{H}_{5.5}\text{btp})_2(\text{H}_6\text{btp})_2(\text{H}_2\text{O})_{12}] \cdot 23.5\text{H}_2\text{O} \cdot \text{MeOH}$ (**1Eu**), recorded at ambient temperature (black line) and at 12 K (red line), with the excitation fixed at 393 nm. The inset shows the $\text{Eu}^{3+} {}^5\text{D}_1 \rightarrow {}^7\text{F}_{0,1,2}$ transitions region recorded at 12 K using excitation wavelengths of 393 (red line) and 310 nm (magenta line).

3. Materials and Methods

3.1. Synthesis of $[\text{Ln}_7(\text{H}_5\text{btp})_4(\text{H}_{5.5}\text{btp})_2(\text{H}_6\text{btp})_2(\text{H}_2\text{O})_{12}] \cdot 23.5\text{H}_2\text{O} \cdot \text{MeOH}$ (**1**)

Reactive mixtures composed of the respective lanthanide(III) chloride hydrates $[\text{LnCl}_3 \cdot 6\text{H}_2\text{O}]$, where $\text{Ln}^{3+} = \text{Eu}^{3+}$ (**1Eu**) and Gd^{3+} (**1Gd**) and 0.025 g of [1,1'-biphenyl]-3,3',5,5'-tetrayltetrakis(phosphonic acid) (**H₈btp**), with an overall molar ratio of approximately 1:4 (**H₈btp**: Ln^{3+}), were individually prepared at ambient temperature in a mixture of distilled water, HCl (6 M) and methanol (2 mL each solvent), and placed inside a 10 mL IntelliVent microwave reactor. The reaction took place inside a CEM Focused Microwave Synthesis System Discover S-Class equipment, under constant magnetic stirring (controlled by the microwave equipment), at 100 °C for 60 min (using an irradiation power of 50 W). A constant flow of air (ca. 20–30 psi of pressure) ensured a close control of the temperature inside the reactor. After irradiation, the reactors with the homogeneous solutions were uncapped and left motionless until ca. 3/4 of the reaction mixture volume had evaporated. This methodology successfully led to the preparation of

[Ln₇(H₅btp)₄(H_{5.5}btp)₂(H₆btp)₂(H₂O)₁₂].23.5H₂O·MeOH (**1Eu** and **1Gd**) materials as white crystalline plates. The resulting compounds were recovered by vacuum filtration, washed with copious amounts of distilled water and then air-dried at ambient temperature.

For [Gd₇(H₅btp)₄(H_{5.5}btp)₂(H₆btp)₂(H₂O)₁₂].23.5H₂O·MeOH

Elemental CH composition (%): Calcd: C 21.0; H 3.01. Found: C 19.9; H 3.02.

Thermogravimetric analysis (TGA) data (weight losses in %) and derivative thermogravimetric peaks (DGT; in italics inside parentheses): 25–100 °C (89 °C) –8.2%; 100–200 °C (179 °C) –4.3%; 200–440 °C (410 °C) –7.4%; 440–800 °C (503 °C) –20.1%

Selected FT-IR data (in cm⁻¹; from KBr pellets): ν(H₂O + POH) = 3600–2800br; ν(C=C) + δ(H₂O) = 1745–1560m; ν(P=O) = 1300–1070vs; ν(P–O) = 1070–830vs; ν(P–C) = 695m.

3.2. Synthesis of [Ln₄(H₃btp)(H₄btp)(H₅btp)(H₂O)₈].3H₂O (**2**)

Reactive mixtures composed of the respective lanthanide(III) chloride hydrates [LnCl₃·6H₂O, where Ln³⁺ = Ce³⁺ (**2Ce**), Pr³⁺ (**2Pr**), and Nd³⁺ (**2Nd**)] and 0.025 g of [1,1'-biphenyl]-3,3',5,5'-tetrayltetrakis(phosphonic acid) (**H₈btp**), with an overall molar ratio of approximately 1:4 (H₈btp: Ln³⁺), were individually prepared in a mixture of distilled water, HCl (6 M) and methanol (2 mL each solvent). Mixtures were kept under constant magnetic stirring in open air and ambient temperature for approximately 15 min. The resulting homogeneous suspensions were transferred to Teflon-lined Parr Instrument reaction vessels and placed inside an MMM Venticell oven. The heating program included:

- (i) heating during 48 h up to 140 °C;
- (ii) 24 h uphold of the temperature (140 °C);
- (iii) cooling down during 48 h until ambient temperature.

The resulting materials were isolated as white microcrystalline powders, recovered by vacuum filtration, washed with abundant amounts of distilled water and dried at ambient temperature. Single-crystals of this compound were obtained from different experimental conditions (denoted as **2La**—see the Supporting Information for further details).

Elemental CH composition (%):

Calcd for **2Ce**: C 19.9; H 2.42. Found: C 21.0; H 2.47.

Calcd for **2Pr**: C 19.9; H 2.41. Found: C 20.7; H 2.37.

Calcd for **2Nd**: C 19.8; H 2.40. Found: C 20.7; H 2.41.

Thermogravimetric analysis (TGA) data (weight losses in %) and derivative thermogravimetric peaks (DTG, in italics inside the parentheses):

2Ce: 25–200 °C –18.05% (110 °C); 200–400 °C –5.98% (271 °C). Total loss: 24.0%.

2Pr: 25–122 °C –10.13% (109 °C); 122–200 °C –5.60% (135 °C); 200–294 °C –6.05% (270 °C); 294–400 °C –6.51% (324 °C). Total loss: 28.3%.

2Nd: 25–133 °C –12.78% (108 °C); 133–205 °C –5.92% (144 °C); 205–367 °C –6.58% (281 °C). Total loss: 25.3%.

Selected FT-IR data (in cm⁻¹; from KBr pellets):

2Ce: ν(H₂O + POH) = 3600–2550br; ν(C=C) + δ(H₂O) = 1700–1570m; ν(P=O) = 1270–1060vs; ν(P–O) = 945–840vs; ν(P–C) = 696m.

2Pr: ν(H₂O + POH) = 3610–2570br; ν(C=C) + δ(H₂O) = 1715–1540m; ν(P=O) = 1245–1070vs; ν(P–O) = 945–850vs; ν(P–C) = 696m.

2Nd: ν(H₂O + POH) = 3625–2565br; ν(C=C) + δ(H₂O) = 1695–1560m; ν(P=O) = 1245–1070vs; ν(P–O) = 940–850vs; ν(P–C) = 696m.

3.3. Single-Crystal X-ray Diffraction Studies

Single crystals of compounds [Eu₇(H₅btp)₄(H_{5.5}btp)₂(H₆btp)₂(H₂O)₁₂].23.5H₂O·MeOH (**1Eu**) and [La₄(H₃btp)(H₄btp)(H₅btp)(H₂O)₈].3H₂O (**2La**) were manually harvested from the crystallization vials and immersed in highly viscous FOMBLIN Y perfluoropolyether vacuum oil (LVAC 140/13,

Sigma-Aldrich) to avoid degradation caused by the evaporation of the solvent [40]. Crystals were mounted on either Hampton Research CryoLoops or MiTeGen MicroLoops, typically with the help of a Stemi 2000 stereomicroscope equipped with Carl Zeiss lenses.

X-ray diffraction data for **1Eu** and **2La** were collected at 150(2)K on a Bruker D8 QUEST equipped with Mo K α sealed tube ($\lambda = 0.71073 \text{ \AA}$), a multilayer TRIUMPH X-ray mirror, a PHOTON 100 CMOS detector, and an Oxford Instruments Cryostrem 700+ Series low temperature device. Diffraction images were processed using the software package SAINT+ [41], and data were corrected for absorption by the multiscan semi-empirical method implemented in SADABS 2016/2 [42]. Structures were solved using the algorithm implemented in SHELXT-2014/5 [43], which allowed the immediate location of almost all of the heaviest atoms composing the molecular unit of the two compounds. The remaining missing and misplaced non-hydrogen atoms were located from difference Fourier maps calculated from successive full-matrix least-squares refinement cycles on F^2 using the latest SHELXL from the 2018/3 release [44]. All structural refinements were performed using the graphical interface ShelXle [45].

For **1Eu**, the hydrogen atoms bound to carbon were placed at their idealized positions using the *HFIX 43* in SHELXL-2014, which were included in subsequent refinement cycles with isotropic displacement parameters (U_{iso}) fixed at $1.2 \times U_{\text{eq}}$ of the parent carbon atoms. Hydrogen atoms associated with the terminal –POH groups were placed at their idealized positions using the *HFIX 83* instruction and were refined assuming isotropic thermal displacements parameters (U_{iso}) fixed at $1.5 \times U_{\text{eq}}$ of the parent oxygen atoms. To find which groups should be protonated it was necessary to simultaneously take into account the P–O bond lengths and the possibility of forming hydrogen bonds with neighboring moieties. Two of these –POH groups shared the hydrogen atom with the neighboring phosphonic group. O23 and O33 shared the hydrogen atom with O30 and O38, respectively. These hydrogen atoms were refined with a 50% occupancy rate each.

The crystallization methanol molecule was refined with 50% of occupancy rate. The hydrogen atoms from the methyl and hydroxyl groups were placed at their idealized positions using the *HFIX 137* and *HFIX 83*, respectively, and were included in subsequent refinement cycles with isotropic displacement parameters (U_{iso}) fixed at $1.5 \times U_{\text{eq}}$ of the parent non-hydrogen atoms.

Due to the considerable disorder of the crystallization water molecules, their hydrogen atoms could not be located from difference Fourier maps and no attempts were made to place them in calculated positions. These atoms were, however, included in the empirical formula of the compound (Table 1). The disorder of these water molecules was refined as follow: 30% occupancy rate for O16W and O19W; 40% for O15W, O21W, O22W and O23W; 50% for O10W, O20W, O25W and O26W; 60% for O14W and O17W; 70% for O13W; 80% for O24W; and 85% for O12W. These occupancy factors were fixed in the final structural model but were obtained from a previous unrestrained refinement for each site. All oxygen atoms belonging to the water molecules of crystallization were refined using a common isotropic displacement parameter.

For **2La** the hydrogen atoms bound to carbon were placed at their idealized positions using the *HFIX 43* in SHELXL-2014, which were included in subsequent refinement cycles with isotropic displacement parameters (U_{iso}) fixed at $1.2 \times U_{\text{eq}}$ of the parent carbon atoms. Hydrogen atoms associated with the terminal –POH groups were placed at their idealized positions using the *HFIX 147* instruction and were refined assuming isotropic thermal displacements parameters (U_{iso}) fixed at $1.5 \times U_{\text{eq}}$ of the parent atoms. Two crystallization water molecules, namely O11W and O12W, were disordered and refined with an occupancy rate of 20% and 80% respectively. The hydrogen atoms of all water molecules could not be located from difference Fourier maps and no attempts were made to place them in calculated positions. These atoms were, however, included in the empirical formula of the compound.

Table 1. Crystal data collection and structure refinement details for [Eu₇(H₅btp)₄(H_{5.5}btp)₂(H₆btp)₂(H₂O)₁₂].23.5H₂O·MeOH (**1Eu**) and [La₄(H₅btp)(H₄btp)(H₃btp)(H₂O)₈].3H₂O (**2La**).

	1Eu	2La
Formula	C ₉₇ H ₁₆₆ Eu ₇ O _{132.5} P ₃₂	C ₃₆ H ₅₂ La ₄ O ₄₇ P ₁₂
Formula weight	5507.05	2164.05
Temperature/K	150(2)	150(2)
Crystal system	Monoclinic	Monoclinic
Space group	<i>P</i> 2 ₁ / <i>c</i>	<i>P</i> 2 ₁ / <i>c</i>
<i>a</i> /Å	13.6342(19)	12.5332(16)
<i>b</i> /Å	34.172(5)	24.147(3)
<i>c</i> /Å	19.049(3)	20.852(3)
<i>b</i> /°	93.213(5)	100.037(3)
Volume/Å ³	8861(2)	6213.9(14)
<i>Z</i>	2	4
$\rho_{\text{calc}}/\text{g cm}^{-3}$	2.064	2.313
<i>m</i> (Mo Ka)/mm ⁻¹	2.854	3.122
Crystal type	Colorless plate	Colorless plate
Crystal size/mm	0.20 × 0.10 × 0.02	0.17 × 0.06 × 0.02
θ range (°)	3.52–25.35	3.518–29.13
	−16 ≤ <i>h</i> ≤ 16	−17 ≤ <i>h</i> ≤ 17
Index ranges	−41 ≤ <i>k</i> ≤ 41	−33 ≤ <i>k</i> ≤ 33
	−22 ≤ <i>l</i> ≤ 22	−26 ≤ <i>l</i> ≤ 28
Collected Reflections	243,730	167,012
Independent Reflections	16,181 (<i>R</i> _{int} = 0.1633)	16,687 (<i>R</i> _{int} = 0.0779)
Completeness	99.7% (θ = 25.24)	99.7% (θ = 25.24)
Final <i>R</i> indices [<i>I</i> > 2σ(<i>I</i>)]	<i>R</i> 1 = 0.0639 <i>wR</i> 2 = 0.1327	<i>R</i> 1 = 0.0549 <i>wR</i> 2 = 0.1101
Final <i>R</i> indices (all data)	<i>R</i> 1 = 0.1088 <i>wR</i> 2 = 0.1507	<i>R</i> 1 = 0.0709 <i>wR</i> 2 = 0.1153
Largest diff. peak and hole/eÅ ⁻³	2.005 and −2.108	2.468 and −1.888
	$R1 = \frac{\sum F_0 - F_c }{\sum F_0 }$ $wR2 = \sqrt{\frac{\sum [w(F_0^2 - F_c^2)^2]}{\sum [w(F_0^2)^2]}}$ $w = 1/[\sigma^2(F_0^2) + (mP)^2 + nP] \text{ where } P = (F_0^2 + 2F_c^2)/3$	

The last difference Fourier map synthesis showed: for **1Eu** the highest peak (2.005 eÅ⁻³) located at 0.65 Å from Eu1 and the deepest hole (−2.108 eÅ⁻³) located at 0.13 Å from O24W, while compound **2La** showed the highest peak (2.468 eÅ⁻³) and the deepest hole (−1.888 eÅ⁻³) located at 0.56 Å and 0.90 Å from La4, respectively. Structural drawings have been created using the software package Crystal Impact Diamond [46].

Information concerning crystallographic data collection and structure refinement details is summarized in Table 1. Tables S1–S4 (in the Supporting Information) gather the most significant distances and angles of the lanthanide coordination environments and hydrogen bonding geometric details. Crystallographic data (including structure factors) for the crystal structures of **1Eu** and **2La** have been deposited with the Cambridge Crystallographic Data Centre as supplementary publication data No. 1,964,385 and 1964384, respectively. Copies of the data can be obtained free of charge on application to CCDC, 12 Union Road, Cambridge CB2 2EZ, U.K. FAX: (+44) 1223 336033. E-mail: deposit@ccdc.cam.ac.uk.

4. Conclusions

The rigid tetrapodal organic linker [1,1'-biphenyl]-3,3',5,5'-tetrayltetrakis(phosphonic acid) (**H₈btp**) was used for the preparation of two new isotypical families of lanthanide–organic frameworks: Ln₇(H₅btp)₄(H_{5.5}btp)₂(H₆btp)₂(H₂O)₁₂].23.5H₂O·MeOH [where Ln³⁺ = Eu³⁺ (**1Eu**) and Gd³⁺ (**1Gd**)], and [Ln₄(H₃btp)(H₄btp)(H₅btp)(H₂O)₈].3H₂O [where Ln³⁺ = Ce³⁺ (**2Ce**), Pr³⁺ (**2Pr**), and Nd³⁺ (**2Nd**)].

This work complements our past research efforts using this ligand, particularly that which described in detail the photoluminescent family $[\text{Ln}_4(\text{H}_6\text{btp})_2(\text{H}_4\text{btp})_2(\text{H}_8\text{btp})(\text{H}_2\text{O})_{16}] \cdot 12\text{H}_2\text{O}$ [where $\text{Ln}^{3+} = \text{La}^{3+}$, $(\text{La}_{0.9}\text{Eu}_{0.1})^{3+}$ and $(\text{La}_{0.9}\text{Tb}_{0.1})^{3+}$] [28].

In our previous report we employed microwave-assisted synthesis at 100 °C (60 min at 50 W) followed by slow evaporation over a period of 7 days. Family 1 herein reported followed an identical synthetic procedure, while trying to explore the structural effect when using smaller radii for the lanthanide cations: we note that in our past work photoluminescent materials were only obtained by doping an inert La^{3+} -based matrix. Two-dimensional compact layers were again obtained, in which the ligand-to-metal ratio is greater than unity. This is an important structural aspect because it means that, despite both synthesis contain in the reactive mixtures a great excess of metal centers, the microwave heating procedure followed by slow evaporation seems to favor the inclusion of a large number of solvent molecules, increasing concomitantly the number of supramolecular contacts in the structures. To note that the same experimental conditions using the hydrothermal method do not permit the preparation of this material. As described for $[\text{Ln}_4(\text{H}_6\text{btp})_2(\text{H}_4\text{btp})_2(\text{H}_8\text{btp})(\text{H}_2\text{O})_{16}] \cdot 12\text{H}_2\text{O}$, compound 1 is also formed by compact layers in which organic cylinders are interconnected by the metallic centers. The presence of optically active Eu^{3+} lanthanide centers yielded photoluminescent materials. As for our previous reported material, the presence of several crystallization and coordinated water molecules in the structure accounts for the lower emission of the Eu^{3+} -based material.

Family 2 of compounds is formed by a three-dimensional network in which, comparatively, the ligand-to-metal ratio is below the unity. We achieved this by increasing the temperature to 140 °C and change the synthetic method to the traditional hydro(solvo)thermal one. This strategy, allied to the usage of larger lanthanides, seemed to favor metallic connectivity in detriment to the various supramolecular contacts involving solvent molecules. This new 3D family of compounds is significantly more compact, but it is still formed by organic cylinders interconnected by the metallic centers, as for family 1 and our previously reported $[\text{Ln}_4(\text{H}_6\text{btp})_2(\text{H}_4\text{btp})_2(\text{H}_8\text{btp})(\text{H}_2\text{O})_{16}] \cdot 12\text{H}_2\text{O}$ compounds.

These two families of compound clearly show the importance of a careful selection of the synthetic experimental method. Despite both syntheses start with the same reactive mixtures (with a great excess of metal), the microwave heating procedure followed by slow evaporation seems to favor the inclusion of a large number of solvent molecules. This leads to an increasing of the number of supramolecular contacts in the structures, originating a 2D layered material. On the other hand, hydrothermal synthesis at higher temperature seems to favor metal coordination of a higher number of phosphonic groups, leading to a more compact 3D network.

Future work related to this system is now being currently focused at the selective control of the dimensionality of the networks so to explore various properties, particularly those related with conductivity: the presence of solvent molecules and many protonated phosphonate groups is expected to significantly boost proton conductivity.

Supplementary Materials: Additional crystallographic data: crystallographic tables, powder x-ray diffraction studies, topological studies. Additional characterization data: thermogravimetry, FT-IR, electron microscopy. Additional details on the synthesis and characterization techniques.

Author Contributions: Laboratory research: A.D.G.F. Ideas and concepts: F.A.A.P. and J.P.C.T. Crystal data acquisition and discussion: R.F.M., J.S.B. and F.A.A.P. Photoluminescence studies: D.A. Writing the original draft preparation: A.D.G.F., R.F.M., J.S.B. and D.A. Writing review and editing: J.P.C.T. and F.A.A.P. Supervision of students: J.P.C.T. and F.A.A.P. All authors have read and agreed to the published version of the manuscript.

Funding: This work was developed within the scope of the project CICECO-Aveiro Institute of Materials, UIDB/50011/2020 & UIDP/50011/2020, financed by national funds through the Portuguese Foundation for Science and Technology/MCTES. Thanks are also due to the University of Aveiro and FCT/MCT for the financial support for the QOPNA research Unit (FCT UID/QUI/00062/2019) and CQE (FCT UID/QUI/0100/2019) research units through national funds and, where applicable, co-financed by the FEDER, within the PT2020 Partnership Agreement.

Acknowledgments: FCT is gratefully acknowledged for the Ph.D. grant No. SFRH/BD/84495/2012 (to ADF) and PD/BD/135104/2017 (to JB). RFM also gratefully acknowledge FCT for the Junior Research Position (CEECIND/00553/2017).

Conflicts of Interest: The authors declare no conflict of interest.

References

1. Silva, P.; Vilela, S.M.F.; Tomé, J.P.C.; Paz, F.A.A. Multifunctional metal-organic frameworks: From academia to industrial applications. *Chem. Soc. Rev.* **2015**, *44*, 6774–6803. [[CrossRef](#)] [[PubMed](#)]
2. Li, B.; Wen, H.M.; Cui, Y.J.; Zhou, W.; Qian, G.D.; Chen, B.L. Emerging multifunctional metal-organic framework materials. *Adv. Mater.* **2016**, *28*, 8819–8860. [[CrossRef](#)] [[PubMed](#)]
3. Sanz-Perez, E.S.; Murdock, C.R.; Didas, S.A.; Jones, C.W. Direct capture of CO₂ from ambient air. *Chem. Rev.* **2016**, *116*, 11840–11876. [[CrossRef](#)] [[PubMed](#)]
4. Suh, M.P.; Park, H.J.; Prasad, T.K.; Lim, D.W. Hydrogen storage in metal-organic frameworks. *Chem. Rev.* **2012**, *112*, 782–835. [[CrossRef](#)] [[PubMed](#)]
5. Joharian, M.; Morsali, A.; Tehrani, A.A.; Carlucci, L.; Proserpio, D.M. Water-stable fluorinated metal-organic frameworks (f-mofs) with hydrophobic properties as efficient and highly active heterogeneous catalysts in aqueous solution. *Green Chem.* **2018**, *20*, 5336–5345. [[CrossRef](#)]
6. Huang, Y.B.; Liang, J.; Wang, X.S.; Cao, R. Multifunctional metal-organic framework catalysts: Synergistic catalysis and tandem reactions. *Chem. Soc. Rev.* **2017**, *46*, 126–157. [[CrossRef](#)]
7. Tehrani, A.A.; Esrafil, L.; Abedi, S.; Morsali, A.; Carlucci, L.; Proserpio, D.M.; Wang, J.; Junk, P.C.; Liu, T.F. Urea metal-organic frameworks for nitro-substituted compounds sensing. *Inorg. Chem.* **2017**, *56*, 1446–1454. [[CrossRef](#)]
8. Smith, J.A.; Singh-Wilmot, M.A.; Carter, K.P.; Cahill, C.L.; Ridenour, J.A. Lanthanide-2,3,5,6-tetrabromoterephthalic acid metal-organic frameworks: Evolution of halogen center dot center dot center dot halogen interactions across the lanthanide series and their potential as selective bifunctional sensors for the detection of Fe³⁺, Cu²⁺, and nitroaromatics. *Cryst. Growth Des.* **2019**, *19*, 305–319.
9. Lustig, W.P.; Mukherjee, S.; Rudd, N.D.; Desai, A.V.; Li, J.; Ghosh, S.K. Metal-organic frameworks: Functional luminescent and photonic materials for sensing applications. *Chem. Soc. Rev.* **2017**, *46*, 3242–3285. [[CrossRef](#)]
10. Pereira, C.F.; Figueira, F.; Mendes, R.F.; Rocha, J.; Hupp, J.T.; Farha, O.K.; Simões, M.M.Q.; Tomé, J.P.C.; Paz, F.A.A. Bifunctional porphyrin-based nano-metal-organic frameworks: Catalytic and chemosensing studies. *Inorg. Chem.* **2018**, *57*, 3855–3864. [[CrossRef](#)]
11. Venkatramiah, N.; Pereira, C.F.; Mendes, R.F.; Paz, F.A.A.; Tomé, J.P.C. Phosphonate appended porphyrins as versatile chemosensors for selective detection of trinitrotoluene. *Anal. Chem.* **2015**, *87*, 4515–4522. [[CrossRef](#)] [[PubMed](#)]
12. Chen, W.; Wu, C.S. Synthesis, functionalization, and applications of metal-organic frameworks in biomedicine. *Dalton Trans.* **2018**, *47*, 2114–2133. [[CrossRef](#)] [[PubMed](#)]
13. Horcajada, P.; Gref, R.; Baati, T.; Allan, P.K.; Maurin, G.; Couvreur, P.; Férey, G.; Morris, R.E.; Serre, C. Metal-organic frameworks in biomedicine. *Chem. Rev.* **2012**, *112*, 1232–1268. [[CrossRef](#)] [[PubMed](#)]
14. Dong, J.; Zhao, D.; Lu, Y.; Sun, W.Y. Photoluminescent metal-organic frameworks and their application for sensing biomolecules. *J. Mater. Chem. A* **2019**, *7*, 22744–22767. [[CrossRef](#)]
15. He, J.; Xu, J.L.; Yin, J.C.; Li, N.; Bu, X.H. Recent advances in luminescent metal-organic frameworks for chemical sensors. *Sci. China-Mater.* **2019**, *62*, 1655–1678. [[CrossRef](#)]
16. Kuyuldar, S.; Genna, D.T.; Burda, C. On the potential for nanoscale metal-organic frameworks for energy applications. *J. Mater. Chem. A* **2019**, *7*, 21545–21576. [[CrossRef](#)]
17. Zhang, Z.; Sang, W.; Xie, L.S.; Dai, Y.L. Metal-organic frameworks for multimodal bioimaging and synergistic cancer chemotherapy. *Coord. Chem. Rev.* **2019**, *399*, 213022. [[CrossRef](#)]
18. Bobbitt, N.S.; Mendonça, M.L.; Howarth, A.J.; Islamoglu, T.; Hupp, J.T.; Farha, O.K.; Snurr, R.Q. Metal-organic frameworks for the removal of toxic industrial chemicals and chemical warfare agents. *Chem. Soc. Rev.* **2017**, *46*, 3357–3385. [[CrossRef](#)]
19. Wang, H.L.; Zhu, Q.L.; Zou, R.Q.; Xu, Q. Metal-organic frameworks for energy applications. *Chem* **2017**, *2*, 52–80. [[CrossRef](#)]
20. Colodrero, R.M.P.; Salcedo, I.R.; Bazaga-Garcia, M.; Barouda, E.; Papadaki, M.; Papathanasiou, K.E.; Hernandez-Alonso, D.; Rius, J.; Aranda, M.A.G.; Losilla, E.R.; et al. High-throughput synthesis of pillared-layered magnesium tetrakisphosphate coordination polymers: Framework interconversions and proton conductivity studies. *Inorganics* **2018**, *6*, 96. [[CrossRef](#)]

21. Salcedo, I.R.; Colodrero, R.M.P.; Bazaga-Garcia, M.; Vasileiou, A.; Papadaki, M.; Olivera-Pastor, P.; Infantes-Molina, A.; Losilla, E.R.; Mezei, G.; Cabeza, A.; et al. From light to heavy alkali metal tetraphosphonates (m = li, na, k, rb, cs): Cation size-induced structural diversity and water-facilitated proton conductivity. *Crystengcomm* **2018**, *20*, 7648–7658. [CrossRef]
22. Ji, B.M.; Deng, D.S.; Ma, J.Y.; Sun, C.W.; Zhao, B. Two- and three-dimensional lanthanide-based coordination polymers assembled by the synergistic effect of various lanthanide radii and flexibility of a new binicotinate-containing ligand: In situ synthesis, structures, and properties. *RSC Adv.* **2015**, *5*, 2239–2248. [CrossRef]
23. Xiang, S.C.; Hu, S.M.; Sheng, T.L.; Chen, J.S.; Wu, X.T. Structural diversity of infinite 3d-4f heterometallic cluster compounds driven by various lanthanide radii. *Chem.-Eur. J.* **2009**, *15*, 12496–12502. [CrossRef] [PubMed]
24. Yan, X.H.; Li, Y.F.; Wang, Q.; Huang, X.G.; Zhang, Y.; Gao, C.J.; Liu, W.S.; Tang, Y.; Zhang, H.R.; Shao, Y.L. Two- to one-dimensional: Radii-dependent self-assembly crystal structures and luminescent properties of lanthanide coordination polymers with an amide type semirigid bridging ligand. *Cryst. Growth Des.* **2011**, *11*, 4205–4212. [CrossRef]
25. Wang, H.S.; Li, J.; Li, J.Y.; Wang, K.; Ding, Y.; Xia, X.H. Lanthanide-based metal-organic framework nanosheets with unique fluorescence quenching properties for two-color intracellular adenosine imaging in living cells. *NPG Asia Mater.* **2017**, *9*, e354. [CrossRef]
26. Zareba, J.K. Tetraphenylmethane and tetraphenylsilane as building units of coordination polymers and supramolecular networks—A focus on tetraphosphonates. *Inorg. Chem. Commun.* **2017**, *86*, 172–186. [CrossRef]
27. Zheng, T.; Yang, Z.X.; Gui, D.X.; Liu, Z.Y.; Wang, X.X.; Dai, X.; Liu, S.T.; Zhang, L.J.; Gao, Y.; Chen, L.H.; et al. Overcoming the crystallization and designability issues in the ultrastable zirconium phosphonate framework system. *Nat. Commun.* **2017**, *8*, 15369. [CrossRef]
28. Firmino, A.D.G.; Mendes, R.F.; Ananias, D.; Vilela, S.M.F.; Carlos, L.D.; Tomé, J.P.C.; Rocha, J.; Paz, F.A.A. Microwave synthesis of a photoluminescent metal-organic framework based on a rigid tetraphosphonate linker. *Inorg. Chim. Acta* **2017**, *455*, 584–594. [CrossRef]
29. Mendes, R.F.; Ananias, D.; Carlos, L.D.; Rocha, J.; Paz, F.A.A. Photoluminescent lanthanide–organic framework based on a tetraphosphonic acid linker. *Cryst. Growth Des.* **2017**, *17*, 5191–5199. [CrossRef]
30. Vilela, S.M.F.; Firmino, A.D.G.; Mendes, R.F.; Fernandes, J.A.; Ananias, D.; Valente, A.A.; Ott, H.; Carlos, L.D.; Rocha, J.; Tomé, J.P.C.; et al. Lanthanide–polyphosphonate coordination polymers combining catalytic and photoluminescence properties. *Chem. Commun.* **2013**, *49*, 6400–6402. [CrossRef]
31. Ananias, D.; Firmino, A.D.G.; Mendes, R.F.; Paz, F.A.A.; Nolasco, M.; Carlos, L.D.; Rocha, J. Excimer formation in a terbium metal-organic framework assists luminescence thermometry. *Chem. Mat.* **2017**, *29*, 9547–9554. [CrossRef]
32. Mendes, R.F.; Antunes, M.M.; Silva, P.; Barbosa, P.; Figueiredo, F.; Linden, A.; Rocha, J.; Valente, A.A.; Paz, F.A.A. A lamellar coordination polymer with remarkable catalytic activity. *Chem.-A Eur. J.* **2016**, *22*, 13136–13146. [CrossRef]
33. Mendes, R.F.; Silva, P.; Antunes, M.M.; Valente, A.A.; Paz, F.A.A. Sustainable synthesis of a catalytic active one-dimensional lanthanide–organic coordination polymer. *Chem. Commun.* **2015**, *51*, 10807–10810. [CrossRef] [PubMed]
34. Firmino, A.D.G.; Mendes, R.F.; Antunes, M.M.; Barbosa, P.C.; Vilela, S.M.F.; Valente, A.A.; Figueiredo, F.M.L.; Tomé, J.P.C.; Paz, F.A.A. Robust multifunctional yttrium-based metal organic frameworks with breathing effect. *Inorg. Chem.* **2017**, *56*, 1193–1208. [CrossRef] [PubMed]
35. Alexandrov, E.V.; Blatov, V.A.; Kochetkov, A.V.; Proserpio, D.M. Underlying nets in three-periodic coordination polymers: Topology, taxonomy and prediction from a computer-aided analysis of the cambridge structural database. *Crystengcomm* **2011**, *13*, 3947–3958. [CrossRef]
36. Blatov, V.A.; Shevchenko, A.P.; Proserpio, D.M. Applied topological analysis of crystal structures with the program package topopro. *Cryst. Growth Des.* **2014**, *14*, 3576–3586. [CrossRef]
37. In RCSR (Reticular Chemistry Structure Resource). Available online: <http://rcsr.anu.edu.au/> (accessed on 15 January 2020).
38. In EPINET. Available online: <http://epinet.anu.edu.au> (accessed on 15 January 2020).

39. Bonneau, C.; O’Keeffe, M.; Proserpio, D.M.; Blatov, V.A.; Batten, S.R.; Bourne, S.A.; Lah, M.S.; Eon, J.G.; Hyde, S.T.; Wiggan, S.B.; et al. Deconstruction of crystalline networks into underlying nets: Relevance for terminology guidelines and crystallographic databases. *Cryst. Growth Des.* **2018**, *18*, 3411–3418. [[CrossRef](#)]
40. Kottke, T.; Stalke, D.J. Crystal handling at low temperatures. *Appl. Crystallogr.* **1993**, *26*, 615–619. [[CrossRef](#)]
41. SAINT+. *Data Integration Engine v. 8.37a*[©]; Bruker AXS: Madison, WI, USA, 1997–2015.
42. Krause, L.; Herbst-Irmer, R.; Sheldrick, G.M.; Stalke, D. Comparison of silver and molybdenum microfocus x-ray sources for single-crystal structure determination. *J. Appl. Crystallogr.* **2015**, *48*, 3–10. [[CrossRef](#)]
43. Sheldrick, G.M. Shelxt - integrated space-group and crystal-structure determination. *Acta Cryst. A* **2015**, *71*, 3–8. [[CrossRef](#)]
44. Sheldrick, G.M. Crystal structure refinement with shelxl. *Acta Crystallogr. Sect. C-Struct. Chem.* **2015**, *71*, 3–8. [[CrossRef](#)] [[PubMed](#)]
45. Hübschle, C.B.; Sheldrick, G.M.; Dittrich, B.J. ShelXle: A Qt graphical user interface for SHELXL. *Appl. Crystallogr.* **2011**, *44*, 1281–1284.
46. Brandenburg, K. *DIAMOND, Version 3.2f*; Crystal Impact GbR: Bonn, Germany, 1997–2010.

Sample Availability: Limited amount of samples of the compounds may be available from the authors upon request.



© 2020 by the authors. Licensee MDPI, Basel, Switzerland. This article is an open access article distributed under the terms and conditions of the Creative Commons Attribution (CC BY) license (<http://creativecommons.org/licenses/by/4.0/>).